

Guiding and magneto-optical properties of TGG waveguide by proton implantation combined with femtosecond laser ablation

Chun-Xiao Liu(刘春晓), Zi-Hao Wang(王子昊), Bei-Er Guo(郭贝尔), Rui Yuan(袁睿), Yi-Fan Wang(王逸凡), Yu-Hang Zhou(周雨航), Jia-Bin Sun(孙家彬), Liao-Lin Zhang(张料林), and Hai-Tao Guo(郭海涛)
Citation: Chin. Phys. B, 2025, 34 (**5**): 054207. DOI: 10.1088/1674-1056/adb9cc
http://cpb.iphy.ac.cn; http://iopscience.iop.org/cpb

What follows is a list of articles you may be interested in

Experimental demonstration of silicon nitride waveguide gratings with excellent efficiency and divergence angle

Zhaozhen Chen(陈兆震), Wenling Li(李文玲), Qian Wang(王乾), Enfeng Liu(刘恩峰), Xinqun Zhang(张新群), Jingwei Liu(刘敬伟), and Zhengsheng Han(韩郑生)
Chin. Phys. B, 2025, 34 (**5**): 054206. DOI: 10.1088/1674-1056/adbbbf

Frequency-tunable single-photon router based on a microresonator containing a driven three-level emitter

Jin-Song Huang(黄劲松), Jing-Lan Hu(胡菁兰), Yan-Ling Li(李艳玲), and Zhong-Hui Xu(徐中辉)
Chin. Phys. B, 2024, 33 (**6**): 064202. DOI: 10.1088/1674-1056/ad362a

Singular optical propagation properties of two types of one-dimensional anti-*PT*-symmetric periodic ring optical waveguide networks

Yanglong Fan(樊阳龙), Xiangbo Yang(杨湘波), Huada Lian(练华达), Runkai Chen(陈润楷),Pengbo Zhu(朱蓬勃), Dongmei Deng(邓冬梅), Hongzhan Liu(刘宏展), and Zhongchao Wei(韦中超)
Chin. Phys. B, 2024, 33 (**3**): 034201. DOI: 10.1088/1674-1056/ad12ab

Silicon-based optoelectronic heterogeneous integration for optical interconnection

Le-Liang Li(李乐良), Gui-Ke Li(李贵柯), Zhao Zhang(张钊), Jian Liu(刘剑), Nan-Jian Wu(吴南健), Kai-You Wang(王开友), Nan Qi(祁楠), and Li-Yuan Liu(刘力源)
Chin. Phys. B, 2024, 33 (**2**): 024201. DOI: 10.1088/1674-1056/ad0e5b

Nonlinear perturbation of a high-order exceptional point: Skin discrete breathers and the hierarchical power-law scaling

Hui Jiang(江慧), Enhong Cheng(成恩宏), Ziyu Zhou(周子榆), and Li-Jun Lang(郎利君)
Chin. Phys. B, 2023, 32 (**8**): 084203. DOI: 10.1088/1674-1056/accb47

Guiding and magneto–optical properties of TGG waveguide by proton implantation combined with femtosecond laser ablation

Chun-Xiao Liu(刘春晓)[1,†], Zi-Hao Wang(王子昊)[1], Bei-Er Guo(郭贝尔)[1], Rui Yuan(袁睿)[1], Yi-Fan Wang(王逸凡)[1], Yu-Hang Zhou(周雨航)[1], Jia-Bin Sun(孙家彬)[1], Liao-Lin Zhang(张料林)[2], and Hai-Tao Guo(郭海涛)[3]

[1] *College of Electronic and Optical Engineering, Nanjing University of Posts and Telecommunications, Nanjing* 210023, *China*
[2] *School of Material Science and Engineering, Jiangxi University of Science and Technology, Ganzhou* 341000, *China*
[3] *State Key Laboratory of Transient Optics and Photonics, Xi'an Institute of Optics and Precision Mechanics, Chinese Academy of Sciences (CAS), Xi'an* 710119, *China*

(Received 27 December 2024; revised manuscript received 13 February 2025; accepted manuscript online 25 February 2025)

Integrating the magneto–optical effect into a waveguide-based photonic device becomes more and more interesting. In the work, the planar optical waveguide firstly was prepared in a terbium gallium garnet crystal (TGG) via the proton implantation with the energy of 4×10^{-1} MeV and the fluence of 6×10^{8} ions/μm^2. Subsequently, a femtosecond laser with a central wavelength of 800 nm and a power of 3 mW was used to ablate the surface of the planar waveguide, forming the ridge optical waveguide. The dark-mode curve of the planar waveguide was measured by a prism coupling technique. The top-view morphology of the ridge waveguide was observed via a Nikon microscope. The mode field distributions of the planar and ridge waveguides were obtained by an end-face coupling system, and the propagation losses of the two waveguides were measured to be 2.26 dB/cm and 2.58 dB/cm, respectively. The Verdet constants were measured to be −72.7 °/T·cm for the TGG substrate and −60.7 °/T·cm for the ridge waveguide. The TGG waveguides have a potential in the fabrication of magneto–optical waveguide devices.

Keywords: optical waveguide, ion implantation, terbium gallium garnet crystal (TGG), magneto–optical effect, femtosecond laser ablation

PACS: 42.79.Gn, 61.80.Jh

DOI: 10.1088/1674-1056/adb9cc **CSTR:** 32038.14.CPB.adb9cc

1. Introduction

Magneto–optical materials, with unique optical and magnetic properties, have significantly driven the development of optical communications and high-peak-power lasers. They are crucial materials for fabricating various optical devices, such as modulators, switches and isolators.[1–3] As a novel magneto–optical material, terbium gallium garnet crystal (TGG) has become one of the indispensable materials in many high-performance optical devices and systems.[4] The TGG crystal features a high Verdet constant (e.g., 35 rad·T^{-1}·m^{-1} at 1064 nm), high transmittance, low transmission loss and high laser damage threshold.[5,6] In addition, it also exhibits excellent thermal–optical and mechanical properties.[7] Although they are all based on these high-quality magneto–optical materials, most of the commercial traditional magneto–optical devices are blocky structures, which cannot be integrated into micron-scale optical circuits because of their large size. Therefore, the development of waveguide magneto–optical devices based on TGG crystals is of great significance for the advancement of integrated optics.

A waveguide is a basic component in the integrated optical circuit, which is the preferred component for optical devices to achieve miniaturization and integration.[8–10] It is a light transmission channel where the light wave is confined to the micron-size layer.[11] According to the different dimensions of the transmission beam limited by the waveguide, it contains both one-dimensional (1D) and two-dimensional (2D) structures.[12] Common techniques for constructing 1D waveguides currently include metal ion in-diffusion, femtosecond laser writing, epitaxial film deposition, and ion implantation.[13,14] Ion implantation is a method for the material surface modification.[15] How it induces a change in refractive index can be found in Ref. [16]. It has the advantages of high controllability and wide material applicability.[17,18] Thererfore, the ion implantation has become an efficient method of waveguide preparation, and has been successfully applied in over 100 types of optical materials.[19,20] The 1D waveguides only confine light propagation in one direction, which cannot meet the demand for high-performance integrated optical devices. Therefore, it is necessary to use other micromachining techniques based on 1D waveguides to fabricate more compact and superior-performing ridge waveguides. Competitive fabrication methods include femtosecond (FS) laser ablation and precise diamond blade dicing

[†]Corresponding author. E-mail: chunxiaoliu@njupt.edu.cn

© 2025 Chinese Physical Society and IOP Publishing Ltd. All rights, including for text and data mining, AI training, and similar technologies, are reserved.

techniques.[21,22] In the femtosecond laser ablation process, the FS-laser focused by the microscope objective lens ablates two parallel air grooves on the 1D waveguide surface, and the structure between these two air grooves is the ridge waveguide.[23–25] Compared with precision diamond blade dicing, the FS-laser ablation offers advantages including high processing precision, small heat-affected area, no pollution, and high controllability. Therefore, the construction of 2D TGG waveguides is carried out by the hybrid technique of the ion implantation and FS-laser ablation.

In previous reports, Wang *et al*. implanted silicon ions with a fluence of 2×10^7 ions/μm^2 and an energy of 6 MeV combined with precise diamond blade dicing technology into TGG crystals to prepare ridge optical waveguides, but the magneto–optical properties of waveguides were not studied.[26] In addition, fabricating waveguides that possess both excellent optical performance and the ability to retain the superior magneto–optical properties of the bulk material is one of the key challenges in the current research of waveguide optical isolators. In this work, the planar waveguide is firstly prepared via the 4×10^{-1}-MeV proton implantation with a dose of 6×10^8 ions/μm^2 into the TGG crystal. Subsequently, the ridge optical waveguide is produced using the FS-laser ablation based on the H^+-implanted TGG. The characteristics of the planar waveguide, as well as the optical properties and Faraday rotation effect of the ridge waveguide are studied systematically. To our knowledge, it is the first report that studies the Faraday rotation effect in the proton-implanted and FS-laser ablated TGG waveguide.

2. Experiment

The TGG crystal was produced by CASTECH using the Czochralski method, and its chemical formula is $Tb_3Ga_5O_{12}$. Its maximum surfaces (1 cm×0.5 cm) and the two end-faces (0.5 cm×0.3 cm) were carefully polished. Before ion implantation, the refractive index of the TGG crystal was measured to be 1.9660 at 632.8 nm using the prism coupling system. Subsequently, hydrogen ions were uniformly implanted into the polished TGG crystal on its largest surface (1 cm×0.5 cm). The implantation energy and dose were 4×10^{-1} MeV and 6×10^8 ions/μm^2, respectively. During the implantation process, the ion current density was kept below 1×10^{-15} A/μm^2 to avoid thermal effects on the waveguide performance. In addition, the beam direction was at an angle of 7° from the normal direction of the implanted surface to prevent channeling effects.

The ridge waveguide was fabricated on the H^+-implanted TGG using a Ti^{3+}: sapphire CPA amplification system (Spitfire, Spectrum Physics). The center wavelength of the FS-laser was 0.8 μm, the repetition rate of the output pulse was 1000 Hz, and the pulse width was 1.5×10^{-13} s. The laser power was 3×10^{-3} W, and the pulse energy can be adjusted through a half wave plate and a polarizer. The TGG crystal was positioned on a three-dimensional (3D) adjustable platform, and the FS-laser beam was focused onto the sample surface through an objective lens. The laser scanned across the surface at a speed of 5×10^{-5} m/s, ablating a pair of parallel trenches spaced at a certain distance apart.

The near-field mode distributions of the planar and ridge waveguides were measured via the end-face coupling arrangement on an optical table (OMTOOLS, HGZT-24-12). The dark mode spectra of the TGG planar waveguide were recorded using a prism coupling instrument (Metricon Model 2010, USA). The topographic features of the ridge waveguide were observed by a Nikon microscope with a 400× magnification. The magneto–optical performance testing system was constructed based on the end-face coupling system, as presented in Fig. 1. Using an He–Ne laser as the light source, the incident light passed through a polarizer to become linearly polarized light. After being focused by Objective 1 (20×, N.A. = 0.65), the light was coupled into the optical waveguide through its end-face. The light output from the other end of the optical waveguide was focused through another objective (20×, N.A. = 0.65), then passed through an analyzer, and finally collected via a CCD camera. The transmittance direction of the polarizer was fixed, changing the transmittance direction of the analyzer and observing the light field received by the CCD. The corresponding transmittance angles of the analyzer were recorded when the light field was completely extinguished under the two conditions: with and without the applied magnetic field around the waveguide. The difference between these two angles represented the optical rotation angle of the linearly polarized light after passing through the waveguide under the corresponding magnetic field. In the experiment, a constant magnetic field was provided by placing magnetic rings at both ends of the waveguide, with the magnetic field direction parallel to the direction of light propagation. To avoid errors, the rotation angle was averaged over several measurements.

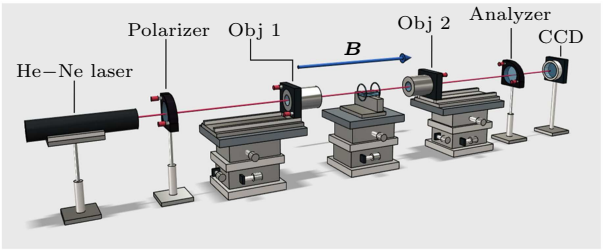


Fig. 1. Schematic diagram of the testing system for Faraday magneto–optical effect.

3. Results and discussion

3.1. Optical properties of the TGG planar waveguide

To analyze the damage caused by ion implantation, SRIM 2013 software[27] is used to simulate and calculate the energy loss distribution for the proton implantation into the TGG. Figure 2 illustrates the relationship between nuclear energy loss and implantation depth. The number of hydrogen ions involved in the simulation is 5×10^4. In the initial phase of the proton range, the nuclear energy loss is small. With the increase of the depth, the irradiated hydrogen ions have elastic collision with the nuclei of the TGG, and the nuclear energy loss gradually increases, reaching a peak loss of 1.2 eV/nm at 2.40 μm. Eventually, a large number of hydrogen ions gradually lose their energy and stop moving, creating a buildup at the end of the proton range. In the deposition region, the volume of the material expands and the density decreases, thus forming an optical barrier structure with the lower refractive index.

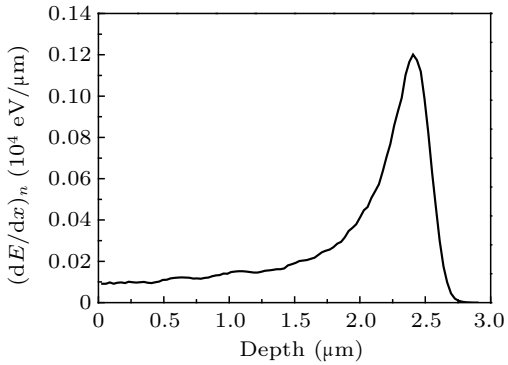


Fig. 2. Energy loss distribution in the TGG during the hydrogen ion implantation.

Figures 3(a) and 3(b) display the dark mode curves of TE and TM polarization modes in the planar waveguide of the TGG crystal implanted with the hydrogen ions at 632.8 nm, respectively. It can be observed from the figures that there are three dips in both polarization modes. Among them, the first dip is relatively sharp, indicating that it is a good guided mode. The second and third dips gradually flatten out at the bottom, which may correspond to the leakage pattern. The effective refractive indices corresponding to the first guided mode (fundamental mode) in TE and TM polarization modes are 1.9669 and 1.9675, both higher than the substrate refractive index of 1.9660. These results indicate that the waveguide formed via the H^+ ions implanted into the TGG with the energy of 4×10^{-1} MeV and the fluence of 6×10^8 ions/μm^2 has a "well + barrier" type structure. In TE polarization mode, the reflected light intensity of the first dip is 27%, which is lower than that of the first guiding mode in TM polarization mode, indicating that the waveguide at 632.8 nm has stronger limiting ability to the light waves in the TE polarization mode.

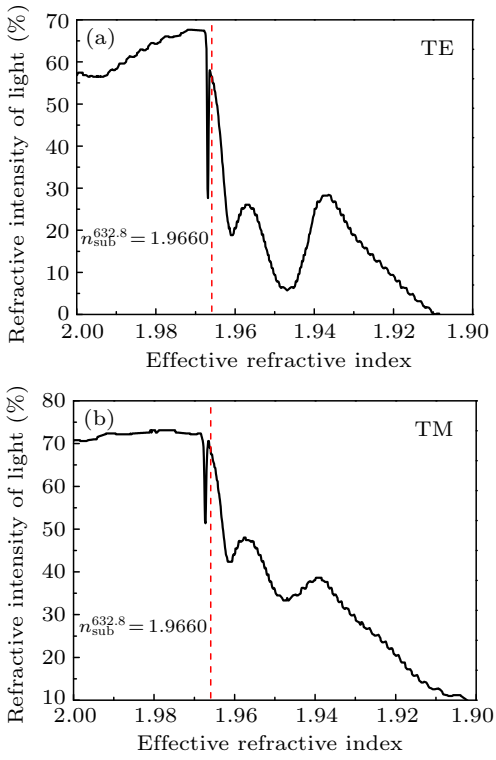


Fig. 3. Dark mode curves of the TGG implanted with hydrogen ions in (a) TE and (b) TM polarization modes.

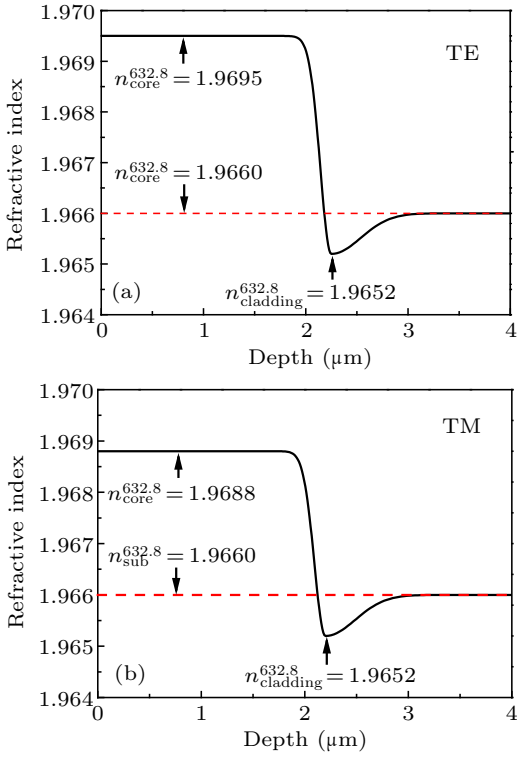


Fig. 4. Refractive index distributions of the TGG planar waveguide implanted with hydrogen ions in (a) TE and (b) TM polarization modes.

The refractive index distribution determines the optical transmission performance of an optical waveguide, which is a significant factor in the study of waveguide characteristics. According to the effective refractive index corresponding to each guided mode in the dark mode curve and the implantation depth calculated by SRIM software, the refractive index dis-

tribution of the proton-implanted TGG planar waveguide was reconstructed by the reflection calculation method (RCM).[28] Figures 4(a) and 4(b) show the refractive index distributions at 6.328×10^{-1} μm in TE and TM polarization modes, respectively. The refractive index within the 0 μm–2.1 μm region has increased, with increases of 0.0035 and 0.0028 for TE and TM polarizations, respectively, compared with the substrate refractive index. The optical barrier region is located in the depth range of 2.1 μm–3.0 μm, and the refractive index is lowest at 2.25 μm, which is 0.001 lower than the TGG refractive index. Therefore, the region of elevated refractive index between the air and the optical barrier can be used as a waveguide core for transmitting light waves. Furthermore, the index difference between the core and the cladding is 0.0043 for TE and 0.0033 for TM, and the effective refractive index of fundamental mode is higher than the lowest refractive index of the barrier. Tables 1 and 2 present comparisons between the experimental and simulated effective refractive indices for the TE and TM polarization modes. The differences between the experimental and simulated values are within the range of 0.0001 to 0.001, indicating that the refractive index profile of the optical waveguide fitted using RCM is reasonable.

Table 1. Comparisons of experimental and simulated effective refractive indices in TE polarization mode of the H^+-implanted TGG planar waveguide.

Mode order	Effective refractive index		
	Measurement	Simulation	Difference
TE_0	1.9669	1.9665	0.0004
TE_1	1.9608	1.9578	0.003
TE_2	1.9468	1.9497	–0.0029

Table 2. Comparisons of experimental and simulated effective refractive indices in TM polarization mode of the H^+-implanted TGG planar waveguide.

Mode order	Effective refractive index		
	Measurement	Simulation	Difference
TM_0	1.9675	1.9662	0.0013
TM_1	1.9615	1.9582	0.0033
TM_2	1.9480	1.9507	–0.0027

The guiding properties of optical waveguides directly determine the performance of their waveguide devices. The near-field intensity profile of the TE_0 polarization mode of the TGG planar optical waveguide at 6.328×10^{-1} μm is collected using an end-face coupling setup, as illustrated in Fig. 5(a). Figure 5(b) depicts the simulated near-field intensity profile of the TE_0 polarization mode at 6.328×10^{-1} μm obtained using the FD-BPM.[29] The experimental result has a high similarity with the simulated one, both of which can display a bright and continuous stripe, almost no light leakage phenomenon. The light wave is well confined in the waveguide layer, and the waveguide has excellent light conduction performance. In addition, the longitudinal limit range of the waveguide is about 2.2 μm, which is basically consistent with the peak position of nuclear energy loss. It proves that the nuclear energy loss is the main cause of the refractive index change.

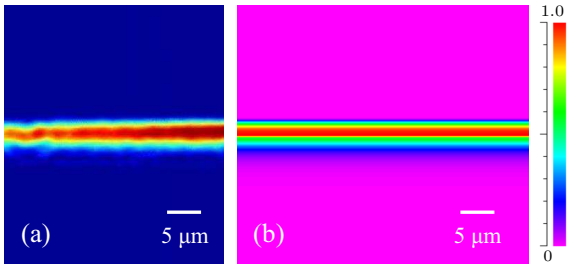


Fig. 5. (a) Measured and (b) simulated near-field light intensity distributions of the H^+-implanted TGG planar optical waveguide.

3.2. Optical and magneto–optical properties of TGG ridge waveguide

The ridge waveguide with the width of 20 μm was prepared on the surface of the H^+-implanted TGG planar waveguide via the femtosecond laser ablation technique along the light propagation direction. Figure 6 is the top-view of the ridge waveguide taken by a Nikon microscope. There are a few black spots on the upper surface of the ridge waveguide, possibly due to the laser scanning at a slow speed, causing prolonged exposure to the material surface and resulting in thermal effects. It should be noted that in the ablation process, the groove depth is larger than the waveguide thickness.

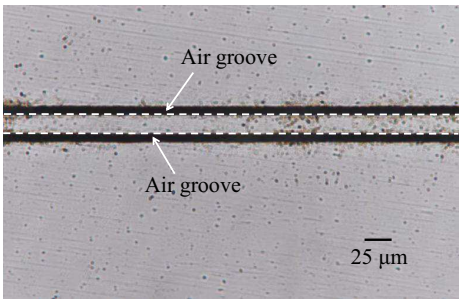


Fig. 6. Top-view of the TGG ridge waveguide prepared by the FS-laser ablation.

The near-field intensity profile of the 20-μm wide ridge waveguide on the TGG crystal is measured via the end-face coupling device, as demonstrated in Fig. 7(a). It can be observed that the ridge waveguide can limit the beam propagation in the vertical and horizontal directions at the same time, which can transmit the light wave with a wavelength of 6.328×10^{-1} μm well. Slight light leakage may be caused by the poor polishing on the end face. Figure 7(b) reveals the mode field image of the ridge waveguide simulated via the FD-BPM. It can be found that there is a high degree of similarity with the actual measurement result, which also suggests that the refractive index distribution reconstructed by the RCM is reasonable. Based on the end-face coupling device, the input and output powers of both the planar and the ridge waveguides

are measured by a power meter (Thorlabs), and the propagation loss is calculated, as shown in Table 3. The propagation losses of the TGG crystal planar and ridge optical waveguides are 2.26 dB/cm and 2.58 dB/cm, respectively.

Table 3. Propagation losses of the TGG planar and ridge waveguides.

	P_{in} (mW)	P_{out} (mW)	α (dB/cm)
Planar waveguide	3.7	2.2	2.26
Ridge waveguide	3.8	2.1	2.58

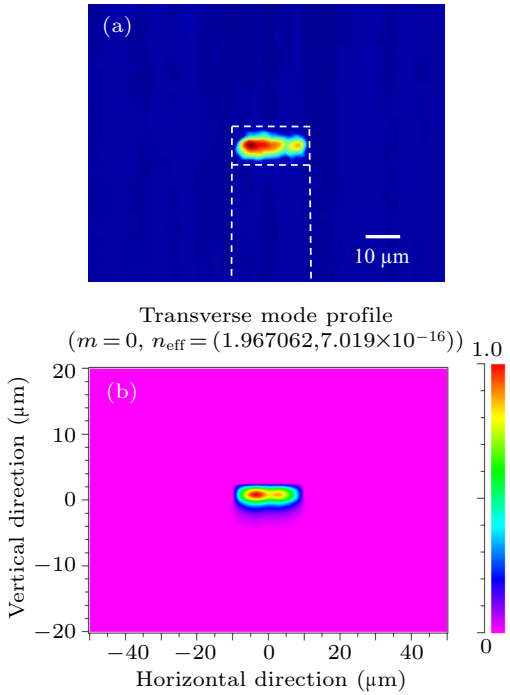


Fig. 7. (a) Measured and (b) simulated near-field intensity profiles of the TGG ridge waveguide.

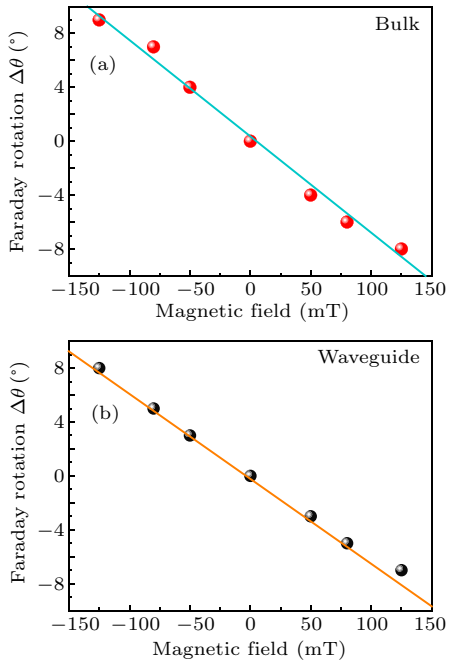


Fig. 8. The linear variation of Faraday rotation angle of (a) the TGG substrate and (b) the ridge waveguide with the applied magnetic field.

The magneto–optical response characteristics are important for magneto–optical devices[32–35] The phase mismatch between the TE and TM orthogonal modes can be ignored, and the Faraday rotation effect can occur in the TGG ridge waveguide under an external magnetic field. In order to investigate the Faraday rotation performances, the rotation angles of the substrate and the ridge waveguide of the TGG crystal under different magnetic field intensities are measured, and then a straight line is fitted by a least square method to calculate the corresponding Verdet constant, as shown in Fig. 8. The Verdet constants obtained for the substrate and the ridge waveguide are -72.7 °/T·cm and -60.7 °/T·cm, respectively. The waveguide region exhibits a slightly lower Verdet constant compared with the substrate, yet it largely retains the magneto–optical properties of the bulk material. It demonstrates the potential for fabricating high-performance waveguide magneto–optical devices.

4. Conclusion

The planar waveguide was prepared via the hydrogen ion implantation at the energy of 4×10^{-1} MeV and the fluence of 6×10^{8} ions/μm^2 on the TGG crystal, and the ridge waveguide was fabricated by the FS-laser ablation technique. The mechanism of the waveguide formation by the ion implantation was analyzed via the SRIM software. It is found that the nuclear energy loss reaches a peak at 2.4 μm, and the optical barrier with the reduced refractive index is formed. The refractive index distribution of the planar waveguide was fitted with the RCM, and the waveguide structure is a typical "well + barrier" type. The near-field light intensity distributions of the planar and ridge waveguides at 6.328×10^{-1} μm were measured via the end-face coupling system. The results suggest that the two waveguides can effectively limit the beam transmission, and the propagation losses of the two waveguides are 2.26 dB/cm and 2.58 dB/cm, respectively. The Verdet constants in the TGG substrate and the ridge waveguide are -72.7 °/T·cm and -60.7 °/T·cm, based on the end-coupling system. This indicates that the ridge waveguide effectively preserves the excellent Faraday rotation characteristics of the TGG crystal. These findings establish a foundation for developing micron-sized magneto–optical devices.

Acknowledgements

Project supported by the Postgraduate Research and Innovation Program of Jiangsu Province, China (Grant No. KYCX24_1133), the National Natural Science Foundation of China (Grant No. 11405041), the Key Research and Development Program of Jiangxi Province, China (Grant No. 20223BBE51020), and the Opening Fund of Key Laboratory of Rare Earths (Chinese Academy of Sciences).

References

[1] Carothers K J, Norwood R A and Pyun J 2022 *Chem. Mater.* **34** 2531

[2] Pintus P, Ranzani L, Pinna S, Huang D, Gustafsson M V, Karinou F, Casula G A, Shoji Y, Takamura Y, Mizumoto T, Soltani M and Bowers J E 2022 *Nat. Electron.* **5** 604

[3] Shoji Y and Mizumoto T 2018 *Opt. Mater. Express* **8** 2387

[4] Chen T B, Yu Y X, Li L C, Zhu J, Cong M H and Song J Y 2021 *J. Cryst. Growth* **562** 126090

[5] Wu Z, Zhang Z H, Zhang Z, Zhou S Y, Su L B and Wu A H 2024 *Chin. J. Quantum Electron.* **41** 194 (in Chinese)

[6] Jin W Z, Ding J X, Guo L, Gu Q, Li C, Su L B, Wu A H and Zeng F M 2018 *J. Cryst. Growth* **484** 17

[7] Snetkov I and Li J 2022 *Magnetochemistry* **8** 168

[8] Chen S, Zhuo M P, Wang X D, Wei G Q and Liao L S 2021 *PhotoniX* **2** 1

[9] Fan Y L, Yang X B, Lian H D, Chen R K, Zhu P B, Deng D M, Liu H Z and Wei Z C 2024 *Chin. Phys. B* **33** 034201

[10] Zhao D, Fan F, Li T F, Tan Z Y, Cheng J R and Chang S J 2022 *Sci. China Inf. Sci.* **65** 169401

[11] Okamoto K 2021 *Fundamentals of optical waveguides* (Amsterdam: Elsevier) p. 15

[12] Lu Y, Yin H Y, Chen B K, Zhang L L, Fu L L, Yue Q Y, Zheng R L, Lin S B and Liu C X 2022 *Mod. Phys. Lett. B* **36** 2150581

[13] Bazzan M and Sada C 2015 *Appl. Phys. Rev.* **2** 040603

[14] Minemura D, Kou R, Sutoh Y, Murai T, Yamada K and Shoji Y 2023 *Opt. Express* **31** 27821

[15] Huang L Q, Wu H Y, Cai G X, Wu S X, Li D R, Jiang T, Qiao B Y, Jiang C Z and Ren F 2024 *ACS Nano* **18** 2578

[16] Pan H, Shi W H, Zhang Z X, Chen H Y, Fu L L, Zhang L L, Lin S B and Liu C X 2023 *J. Mater. Sci.: Mater. Electron.* **34** 1091

[17] You J L, Wang Y S, Wang T, Zhang L L, Fu L L, Yue Q Y, Wang X F, Zheng R L and Liu C X 2022 *Chin. Phys. B* **31** 114203

[18] Liu C X, Liu T, Liu X H, Wei W and Peng B 2011 *Chin. Phys. Lett.* **28** 114205

[19] Chen F, Amekura H and Jia Y C 2020 *Ion irradiation of dielectrics for photonic applications* (Singapore: Springer-Nature) pp. 7–10

[20] Zhao J, Ni X, Huo Y Y, Sun W, Zhang L L and Liu C X 2024 *Phys. Scr.* **99** 055560

[21] He S, Zhang Z Y, Liu H L, Akhmadaliev S, Zhou S Q, Wang X P and Wu P F 2019 *Appl. Phys. Express* **12** 076502

[22] Xu H, Li Z Q, Pang C, Li R, Li G L, Akhmadaliev Sh, Zhou S Q, Lu Q M, Jia Y C and Chen F 2022 *Chin. Phys. B* **31** 094209

[23] Chen F and Aldana J R V de 2014 *Laser Photon. Rev.* **8** 251

[24] Zhang J, Zhang Y, Xu J, Lin S B and Liu C X 2020 *Vacuum* **172** 109093

[25] Peyton R, Guarepi V, Videla F and Torchia G A 2020 *Opt. Laser Technol.* **125** 106059

[26] Wang Y, Shen X L, Zhu Q F and Liu C X 2018 *Opt. Mater. Express* **8** 3288

[27] Ziegler J F 2023 *SRIM—The Stopping and Range of Ions in Matter* http://www.srim.org

[28] Chandler P J and Lama F L 1986 *Opt. Acta* **33** 127

[29] Rsoft Design Group 2023 *Computer software BeamPROP version* 8.0 http://www.rsoftdesign.com

[30] Liu C X, Sun W, Zhang J Y, Fu L L, Yun L and Zhang L L 2024 *Opt. Eng.* **63** 017102

[31] Liu C X, Zhao J, Hua Z Y, Yang Y C, Sun W, Zhang L L and Wang X F 2023 *Results Phys.* **54** 107103

[32] Zhao D, Fan F, Xue Q, Wang H, Ji Y Y, Yang Q H, Wen Q Y and Chang S J 2024 *Adv. Funct. Mater.* **34** 2404881

[33] Zhao D, Fan F, Tan Z Y, Wang H and Chang S J 2023 *Laser Photon. Rev.* **17** 2200509

[34] Tan Z Y, Fan F, Zhao D, Wang H, Li S S, Guan S N, Cheng J R, Ji Y Y and Chang S J 2024 *Laser Photon. Rev.* **18** 2301008

[35] Zhao D, Fan F, Liu J Y, Tan Z Y, Wang H, Yang Q H, Wen Q Y and Chang S J 2023 *Optica* **10** 1295